A Unified Procedure for Calibrating Intrinsic Parameters of Spherical Lenses

S. S. Beauchemin, R. Bajcsy and G. Givaty
GRASP Laboratory
Department of Computer and Information Science
University of Pennsylvania
Philadelphia PA 19104-6228 USA

Abstract

Spherical cameras are variable-resolution imaging systems that have been recognized as promising devices for autonomous navigation purposes, mainly because of their wide viewing angle which increases the capabilities of vision-based obstacle avoidance schemes. In addition, spherical lenses resemble the primate eye in their projective models and are biologically relevant. We present a novel method for spherical-lens camera calibration which models the lens radial and tangential distortions and determines the optical center and the angular deviations of the CCD sensor array within a unified numerical procedure. Contrary to other methods, there is no need for special equipment such as low-power laser beams or non-standard numerical procedures for finding the optical center. Numerical experiments and analyses are presented.

1 Introduction

Spherical cameras are variable-resolution imaging systems that are recognized as promising devices for autonomous navigation purposes, mainly because of their wide viewing angle which increases the capabilities of vision-based obstacle avoidance schemes [11]. In addition, spherical lenses resemble the primate eye in their projective models and are biologically relevant [4]. In spite of this, the calibration of spherical lenses is not well understood [10] and contributions to this topic have only recently begun to appear in the literature.

Current standard procedures for pinhole camera calibration are inadequate for spherical lenses as such devices introduce significant amounts of image distortion. Calibration methods such as Tsai's [13] only consider the first term of radial distortion which is insufficient to account for the distortion typically induced by spherical lenses. Other calibration procedures for high distortion and spherical lenses such as Shah and Aggarwal's [9] and Basu and Licradie's [3] have been defined. However, these methods use special equipment such as low-power laser beams or ad-hoc numerical procedures for determining the optical center of spherical lenses. We propose a novel method which only requires an adequate calibration plane and a unified numerical procedure for determining the optical center, among other intrinsic parameters.

1.1 Types of Distortion

The calibration of optical sensors in computer vision is an important issue in autonomous navigation, stereo vision and numerous other applications where accurate positional observations are required. Various techniques have been developed for the calibration of sensors based on the traditional pinhole camera model. Typically, the following types of geometrical distortion have been recognized and dealt with [14]:

- **Radial Distortion:** This type of distortion is point-symmetric at the optical center of the lens and causes an inward or outward shift of image points from their initial perspective projection. About the optical center, radial distortion is expressed as

$$\hat{r} = r + \kappa_1 r^3 + \kappa_2 r^5 + \kappa_3 r^7 + \cdots, \qquad (1.1)$$

  where κ_i are radial distortion coefficients, r is the observed radial component of a projected point and $\hat{r}$, its predicted perspective projection [7].

- **Decentering Distortion:** The misalignment of the optical centers of various lens elements in the sensor induces a decentering distortion which has both a radial and a tangential component. They are expressed as

$$\begin{aligned} \hat{r} &= r + 3(\eta_1 r^2 + \eta_2 r^4 + \eta_3 r^6 + \cdots)\sin(\theta - \theta_0) \\ \hat{\theta} &= \theta + (\eta_1 r^2 + \eta_2 r^4 + \eta_3 r^6 + \cdots)\cos(\theta - \theta_0), \end{aligned}$$

where η_i are the decentering distortion coefficients, θ is the observed angular component of a projected point, $\hat{\theta}$ is its predicted perspective projection and θ_0 is the angle between the positive y-axis and the axis of maximum tangential distortion due to decentering [7].

- **Thin Prism:** Manufacturing imperfections of lens elements and misalignment of CCD sensor arrays from their ideal, perpendicular orientation to the optical axis introduce additional radial and tangential distortions which are given by

$$\begin{aligned} \hat{r} &= r + (\zeta_1 r^2 + \zeta_2 r^4 + \zeta_3 r^6 + \cdots)\sin(\theta - \theta_1) \\ \hat{\theta} &= \theta + (\zeta_1 r^2 + \zeta_2 r^4 + \zeta_3 r^6 + \cdots)\cos(\theta - \theta_1), \end{aligned}$$

where ζ_i are the thin prism distortion coefficients and θ_1 is the angle between the positive y-axis and the axis of maximum tangential distortion due to thin prism [7].

1.2 Related Literature

The need for foveated visual fields in active vision applications has motivated the design of special purpose spherical lenses [4] and catadioptric sensors [2]. These imaging systems introduce significant amounts of radial and possibly tangential distortions (see Figure 2.1) and traditional methods that only calibrate for the perspective projection matrix and neglect to compensate for these distortions are inadequate [12].

The calibration methods designed for high-distortion lenses typically model the radial and tangential distortion components with polynomial curve-fitting. Examples of such methods are Shah and Aggarwal's [10] and Basu and Licardie's [3]. Both of these methods calibrate the optical center by using procedures that are not elegantly integrated into the curve-fitting procedure which recovers distortion coefficients. For instance, Basu and Licaride's method consists of a minimization of vertical and horizontal calibration-line curvatures whereas Shah and Aggarwal's requires the use of a low-power laser beam based on a partial reflection beam-alignment technique.

Other, similar methods perform minimizations of functionals representing measures of the the accuracy of the image transformation with respect to calibration parameters [6, 14]. These methods rely on the point-symmetry of radial distortion at the location of the optical center onto the image plane to reduce the dimensionality of the parameter space [6] or to iteratively refine calibration parameters initially obtained with a distortion-free pinhole camera model [14].

In addition to these calibration techniques, Miyamoto [5] defined mappings relating the world plane angle θ_1 to the image plane angle θ_2. One such mapping is given by $\theta_2 = \tan\theta_1$. Alternatively, Anderson *et al.* [1] defined a similar mapping, this time based on Snell's law of diffraction. Unfortunately, the accuracy of these models is limited to the neighborood of the optical center [10]. Basu and Licardie also proposed alternative models for fish-eye lenses [3] but they demonstrate that the small number of calibration parameters involved does not allow to accurately model a spherical lens.

2 Standard Procedure for Fish-Eye Lens Calibration

The number of free intrinsic parameters for a typical high distortion lens is large, especially when one considers sources or radial distortions, decentering and thin prism, manufacturing misalignments such as tilt, yaw and roll angles of the CCD sensor array with respect to its ideal position, image center versus optical center, *etc.* We encompass radial and tangential distortions in two polynomials for which the coefficients are to be determined with respect to the sources of distortion emanating from the location of the optical center and the pitch and yaw angles of the CCD sensor. We proceed by describing the least-squares method chosen to perform the polynomial fits for both radial and tangential distortions.

2.1 Radial and Tangential Polynomials

Given a set of calibration points and their image locations, the equations describing the transformation from fish-eye to pinhole are

$$\hat{\theta}_{ij} = \sum_{k=0}^{L} a_k \theta_{ij}^k \quad \text{and} \quad \hat{r}_{ij} = \sum_{k=0}^{L} b_k r_{ij}^k \qquad (2.2)$$

where L is the order of the polynomials and $\hat{\theta}_{ij}$ and $\hat{r}_{ij}$ are the corrected polar coordinates of the calibration points. We use a calibration pattern for which the points align into horizontal, diagonal and vertical lines. These n^2 calibration points may be arranged in matrix form consistent with their geometric location on the calibration plane. We use the notation $\mathbf{P}_{ij} = (X_{ij}, Y_{ij}, Z_{ij})$ for the 3D calibration points expressed in the coordinate system of the camera, $\hat{\mathbf{p}}_{ij} = (\hat{r}_{ij}, \hat{\theta}_{ij})$ for the 2D projection of $\mathbf{P}_{ij}$ onto the pinhole camera and $\mathbf{p}_{ij} = (r_{ij}, \theta_{ij})$ for the projection of $\mathbf{P}_{ij}$ as imaged by the spherical lens.

Various minimization methods may be applied to the polynomials in order to determine their coefficients. For instance, Lagrangian minimization and

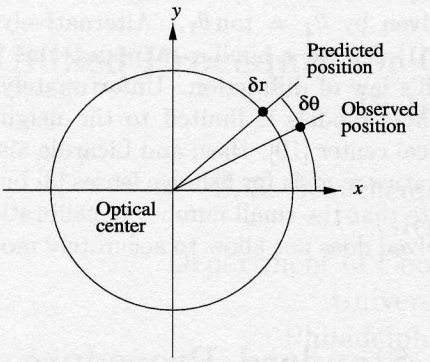

Figure 2.1: *Radial and tangential distortions. The original point, expressed as (r, θ) is the expected observation. The distorted point as observed, is expressed as $(r + \delta r, \theta + \delta\theta)$, where δr and $\delta\theta$ are the radial and tangential distortions, respectively.*

least-squares have been used. For our purposes, we adopt a least-squares approach to find the polynomial coefficients and perform the correction. This least-squares fit for the radial and tangential distortion polynomial can be expressed as

$$\sum_{i=1}^{n}\sum_{j=1}^{n}\left(\hat{\theta}_{ij} - \sum_{k=0}^{L} a_k \theta_{ij}^k\right)^2 \sum_{i=1}^{n}\sum_{j=1}^{n}\left(\hat{r}_{ij} - \sum_{k=0}^{L} b_k r_{ij}^k\right)^2. \tag{2.3}$$

Deriving the polynomials with respect to coefficients yields the following systems of linear equations

$$\mathbf{a}^T\boldsymbol{\Theta} = \theta_{ij}\boldsymbol{\theta}_{ij} \quad \text{and} \quad \mathbf{b}^T\mathbf{R}_{ij} = \hat{r}_{ij}\mathbf{r}_{ij} \tag{2.4}$$

where $\mathbf{a} = (a_0, \ldots, a_L)^T$, $\mathbf{b} = (b_0, \ldots, b_L)^T$, $\mathbf{r}_{ij} = (r_{ij}^0, \ldots, r_{ij}^L)^T$, $\boldsymbol{\theta}_{ij} = (\theta_{ij}^0, \ldots, \theta_{ij}^L)^T$, $\mathbf{R}_{ij} = \mathbf{r}_{ij}\mathbf{r}_{ij}^T$ and $\boldsymbol{\Theta}_{ij} = \boldsymbol{\theta}_{ij}\boldsymbol{\theta}_{ij}^T$. We write the least-squares matrices $\mathbf{A}_r$ and $\mathbf{A}_\theta$ as

$$\begin{pmatrix} r_{11}^0 & \cdots & r_{11}^L \\ r_{12}^0 & \cdots & r_{12}^L \\ \vdots & \vdots & \vdots \\ r_{1n}^0 & \cdots & r_{1n}^L \\ r_{21}^0 & \cdots & r_{2n}^L \\ \vdots & \vdots & \vdots \\ r_{nn}^0 & \cdots & r_{nn}^L \end{pmatrix} \quad \begin{pmatrix} \theta_{11}^0 & \cdots & \theta_{11}^L \\ \theta_{12}^0 & \cdots & \theta_{12}^L \\ \vdots & \vdots & \vdots \\ \theta_{1n}^0 & \cdots & \theta_{1n}^L \\ \theta_{21}^0 & \cdots & \theta_{2n}^L \\ \vdots & \vdots & \vdots \\ \theta_{nn}^0 & \cdots & \theta_{nn}^L \end{pmatrix} \tag{2.5}$$

and we form the least-squares systems of equations as $\mathbf{R}_\theta\mathbf{a} = \boldsymbol{\theta}$ and $\mathbf{R}_r\mathbf{b} = \mathbf{r}$, where $\mathbf{R}_\theta = \mathbf{A}_\theta^T\mathbf{A}_\theta$, $\mathbf{R}_r = \mathbf{A}_r^T\mathbf{A}_r$, $\mathbf{r} = \mathbf{A}_r^T\mathbf{c}_r$, $\boldsymbol{\theta} = \mathbf{A}_\theta^T\mathbf{c}_\theta$, $\mathbf{c}_\theta = (\hat{\theta}_{11}, \hat{\theta}_{12}, \ldots, \hat{\theta}_{nn})$ and $\mathbf{c}_r = (\hat{r}_{11}, \hat{r}_{12}, \ldots, \hat{r}_{nn})$. The coefficients $\mathbf{a}$ and $\mathbf{b}$ are such that they should minimze $\chi_\theta^2 = |\mathbf{A}_\theta\mathbf{a} - \mathbf{c}_\theta|^2$ and $\chi_r^2 = |\mathbf{A}_r\mathbf{b} - \mathbf{c}_r|^2$. We use Singular Value Decomposition (SVD) to perform the least-squares fits

$$\mathbf{a} = \mathbf{V}_\theta \text{diag}(\mathbf{W}_\theta)(\mathbf{U}_\theta^T\mathbf{c}_\theta) \tag{2.6}$$

$$\mathbf{b} = \mathbf{V}_\mathbf{r} \text{diag}(\mathbf{W}_r)(\mathbf{U}_r^T\mathbf{c}_r) \tag{2.7}$$

where $\mathbf{A}_\theta = \mathbf{U}_\theta\mathbf{W}_\theta\mathbf{V}_\theta^T$ and $\mathbf{A}_r = \mathbf{U}_r\mathbf{W}_r\mathbf{V}_r^T$, and to compute χ_θ^2 and χ_r^2. We use the notation $\mathbf{a}(\mathbf{x}_c, \mathbf{x}_p)$, $\mathbf{b}(\mathbf{x}_c, \mathbf{x}_p, \theta_\mathbf{u}, \theta_\mathbf{v})$, $\chi_\theta^2(\mathbf{x}_c, \mathbf{x}_p)$ and $\chi_r^2(\mathbf{x}_c, \mathbf{x}_p, \theta_\mathbf{u}, \theta_\mathbf{v})$ to indicate that the least-squares solutions for tangential distortion coefficients $\mathbf{a}$ and the residual χ_θ^2 depend on $\mathbf{x}_c$, the location of the optical center with respect to the coordinate system in which the fit is performed and $\mathbf{x}_p$, the translation parallel to the calibration surface, and that the radial distortion coefficients $\mathbf{b}$ and the residual χ_r^2 depend on the optical center $\mathbf{x}_c$, the camera translation $\mathbf{x}_p$ and $\theta_\mathbf{u}$ and $\theta_\mathbf{v}$, the pitch and yaw angles of the CCD sensor array with respect to a plane perpendicular to the optical axis. We further explain and experimentally demonstrate these dependencies in the next sections.

2.2 Polynomial Order

The overfit of data, or polynomial orders that exceed the intrinsic order of the data, constitutes our primary motivation for using SVD in the least-squares solutions of the polynomial coefficients. For instance, if any of the singular values is less than a tolerance level of 10^{-5}, we set its reciprocal to zero, rather than letting it go to some arbitrarily high value. We thus avoid overfits of the calibration data when solving for $\mathbf{a}(\mathbf{x}_c, \mathbf{x}_p)$ and $\mathbf{b}(\mathbf{x}_c, \mathbf{x}_p, \theta_\mathbf{u}, \theta_\mathbf{v})$ in (2.6) and (2.7). Because of this capability and considering that the computational cost of calibration is usually not critical, we use polynomials of order $L = 12$.

2.3 The Optical Center

The optical center of a lens is defined as the point where the optical axis passing through the lens intersects the image plane of the camera. Alternatively, the optical center is the image point where no distortions appear, radial or tangential. That is to say, where $\hat{r}_{ij} = r_{ij}$ and $\hat{\theta}_{ij} = \theta_{ij}$. In addition, radial distortion is point-symmetric at the optical center and, consequently, the one-dimensional polynomial in r is accurate only when aligned with the optical center. Figure 2.2 shows plots of $(\hat{r}_{ij}, r_{ij})$ and $(\hat{\theta}_{ij}, \theta_{ij})$ at and away from the optical center, in which the point-scattering effect becomes apparent as the polynomial fit is gradually decentered from the optical center. This effect is reflected in the values of $\chi_r^2(\mathbf{x}_c, \mathbf{x}_p, \theta_\mathbf{u}, \theta_\mathbf{v})$ and $\chi_\theta^2(\mathbf{x}_c, \mathbf{x}_p)$ around the optical center, as illustrated by Figure 2.3.

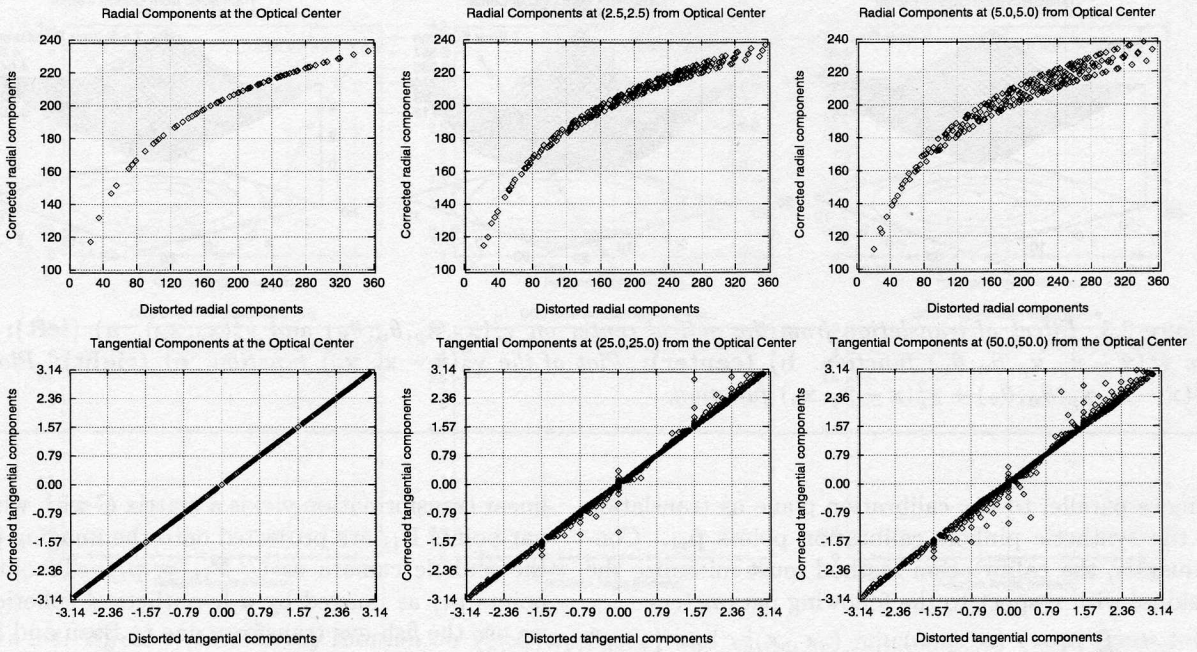

Figure 2.2: *Plots of* $(\hat{r}_{ij}, r_{ij})$ *and* $(\hat{\theta}_{ij}, \theta_{ij})$. **a) (top, from left to right):** $\hat{r}_{ij}$ *and* r_{ij} *at the optical center,* $(2.5, 2.5)$ *and* $(5.0, 5.0)$ *image units away from it.* **b) (bottom, from left to right):** $\hat{\theta}_{ij}$ *and* θ_{ij} *at the optical center,* $(25.0, 25.0)$ *and* $(50.0, 50.0)$ *image units away from it. The increasing scattering of the plots as the distance from the optical center increases prevents accurate modeling of the lens. The effect is most apparent for the* r_{ij} *'s, yet it is also observed with the* θ_{ij} *'s.*

2.4 CCD Sensor Array Misalignments

CCD sensor misalignments are due to imperfections at the time of assembly. Such imperfections, however minute, introduce additional noise as some types of misalignments influence the value of the $\chi^2_r(\mathbf{x}_c, \mathbf{x}_p, \theta_\mathbf{u}, \theta_\mathbf{v})$ function. We have studied the effect of these misalignments by rotating the image plane of the synthetic camera model about its origin. Figure 2.4 shows the $\chi^2_r(\mathbf{x}_c, \mathbf{x}_p, \theta_\mathbf{u}, \theta_\mathbf{v})$ and $\chi^2_\theta(\mathbf{x}_c, \mathbf{x}_p)$ functions for rotations $\theta_\mathbf{u}$, $\theta_\mathbf{v}$ and $\theta_\mathbf{n}$ about the $\mathbf{u}$, $\mathbf{v}$ and $\mathbf{n}$ axes of the synthetic camera. The effects have been studied in isolation to one another and, in these experiments, the optical center projected onto the origin of the synthetic camera.

As expected, rotations about the line of sight axis $\mathbf{n}$ have no effect on the $\chi^2_r(\mathbf{x}_c, \mathbf{x}_p, \theta_\mathbf{u}, \theta_\mathbf{v})$ function, as they do not break the point-symmetry of radial distortion. However, rotations about the axes of the image plane $\mathbf{u}$ and $\mathbf{v}$ introduce errors reflected in $\chi^2_r(\mathbf{x}_c, \mathbf{x}_p, \theta_\mathbf{u}, \theta_\mathbf{v})$ (see Figure 2.4a). As expected, this type of rotation breaks the point-symmetry of radial distortion.

In all three types of rotations, the $\chi^2_\theta(\mathbf{x}_c, \mathbf{x}_p)$ function remains undisturbed, as shown in Figure 2.4b. Since the rotations are such that the position of the optical center is not shifted, no violation of the line-symmetry of the tangential distortion is introduced. If such rotations were to be centered away from the image position of the optical center, then errors would be introduced because of the breaking of line-symmetry. This is also illustrated by Figure 2.5 where, for the three types of rotation, the plots of $(\hat{\theta}_{ij}, \theta_{ij})$ describe a bijection and do not introduce approximation errors in the fit, contrary to the plots of $(\hat{r}_{ij}, r_{ij})$ in Figure 2.2a.

Another phenomenon affecting the value of the residual is the alignment of the synthetic pinhole calibration dots with the spherical points as imaged by the lens. Given an ideal situation in which the central calibration point is imaged at the image center and that this location coincides with the optical center, then the residual is at a minimum. However, any deviation from this situation substantially increases the value of the residual, and for certain is by no means related to the calibration parameters of the camera. Additionally, we cannot require that the central calibration dot be imaged at the optical center, since it is one of the parameters to be estimated.

In light of this, we also model translation of the

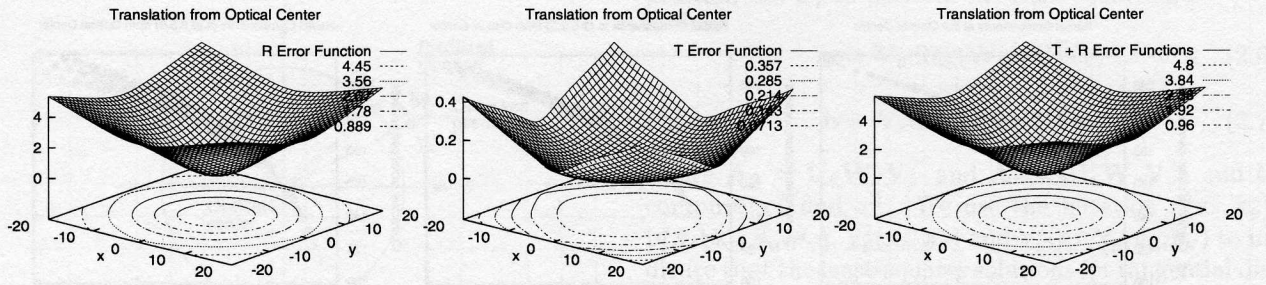

Figure 2.3: *Effect of translation from the optical center on* $\chi_r^2(\mathbf{x}_c, \mathbf{x}_p, \theta_\mathbf{u}, \theta_\mathbf{v})$ *and* $\chi_\theta^2(\mathbf{x}_c, \mathbf{x}_p)$. **a) (left):** *Plot of the* $\chi_r^2(\mathbf{x} - \mathbf{x}_c, \mathbf{x}_p, \theta_\mathbf{u}, \theta_\mathbf{v})$ *function.* **b) (center):** *Plot of the* $\chi_\theta^2(\mathbf{x} - \mathbf{x}_c, \mathbf{x}_p)$ *function.* **c) (right):** *Plot of the* $\chi_r^2(\mathbf{x} - \mathbf{x}_c, \mathbf{x}_p, \theta_\mathbf{u}, \theta_\mathbf{v}) + \chi_\theta^2(\mathbf{x} - \mathbf{x}_c, \mathbf{x}_p)$ *function.*

camera parallel to the calibration plane as translation of the synthetic pinhole calibration points $\hat{\mathbf{p}}_{ij}$. Consequently, the calibrtation method must minimize the residual with respect to the following parameters:

- $\mathbf{x}_c$: The amount of translation of imaged spherical points $\mathbf{p}_{ij}$, which models translation of the CCD sensor array in the $(\mathbf{u}, \mathbf{v})$ plane. In other words, $\mathbf{x}_c$ is the translation from the image center to the optical center.

- $\mathbf{x}_p$: The amount of translation of the synthetic pinhole calibration points $\hat{\mathbf{p}}_{ij}$, which models the translation of the camera in the (X,Y) plane, parallel to the calibration surface.

- $\theta_\mathbf{u}$, $\theta_\mathbf{v}$: The pitch and yaw angles of the CCD sensor array.

3 Synthetic Camera Model

We calibrate against a standard, synthetic pinhole camera described by linear transformation matrices containing the intrinsic parameters to be calibrated. The first transformation is from the world coordinate system to that of the synthetic camera, expressed by the camera position $\mathbf{r}$ in world coordinates and orthogonal unit vectors $\mathbf{u} = (u_x, u_y, u_z)^T$, $\mathbf{v} = (v_x, v_y, v_z)^T$ and $\mathbf{n} = (n_x, n_y, n_z)^T$. In addition, since the vector joining the image plane at the optical center and the focal point may not be perpendicular to the image plane, we model the focal length in the coordinate system of the camera as a vector $\mathbf{f} = (f_u, f_v, f_n)^T$. The translation from optical center to image center $\mathbf{x}_c = (x_c, y_c)^T$ and the scaling factors s_x and s_y from synthetic camera image to real image also are parameters forming the synthetic camera model. Combining these into a homogeneous linear transformation yields a matrix C with which planar points $\mathbf{P}_{ij}$ are projected onto the imaging plane of the pinhole camera as $C^T\mathbf{P}_{ij} = \hat{\mathbf{p}}_{ij}$. To obtain the points $\mathbf{p}_{ij}$ as imaged by a hypothetical spherical lens, we use the fish-eye transform due to Basu and Licardie to distort the $\hat{\mathbf{p}}_{ij}$'s. The fish-eye transformation is given by

$$\mathbf{p}_{ij} = s \log(1 + \lambda \|\hat{\mathbf{p}}_{ij}\|_2) \boldsymbol{\rho}_{ij} \tag{3.8}$$

where $\mathbf{p}_{ij} = (x_{ij}, y_{ij})^T$, $\hat{\mathbf{p}}_{ij} = (\hat{x}_{ij}, \hat{y}_{ij})^T$, $\boldsymbol{\rho}_{ij} = (\cos\xi, \sin\xi)^T$, and $\xi = \arctan \frac{\hat{y}_{ij}}{\hat{x}_{ij}}$. The symbols s and λ are scaling and radial distortion factors, respectively.

4 Description of Algorithm

As a first step, we generate calibration points using the synthetic pinhole camera. The analytic calibration plane is conveniently located in the (X, Y) plane of the world coordinate system and the line of sight of the pinhole camera coincides with its Z axis.

The synthetic image plane is at 340 mm from the calibration plane and the focal length is set to 100 mm. The pinhole calibration points are then projected onto the image plane of the synthetic camera as $C^T\mathbf{P}_{ij} = \hat{\mathbf{p}}_{ij}$ and transformed to polar coordinates as $(\hat{r}_{ij}, \hat{\theta}_{ij})$.

Using the spherical camera, oriented perpendicularly from the real calibration plane, a frame of the calibration points is grabbed. The lens of the spherical camera is at 280 mm from the calibration plane. Figures 5.6a and d show such frames. We perform point detection on this image by computing the centroids of the calibration points and obtain spherical image points (r_{ij}, θ_{ij}). Both sets of points $(\hat{r}_{ij}, \hat{\theta}_{ij})$ and (r_{ij}, θ_{ij}) are scaled to the canonical space $[(-1, -\pi), (1, \pi)]$ where the minimization procedure is to begin.

We use a conjugate gradient minimization procedure due to Polak-Ribiere [8] which we apply on the function

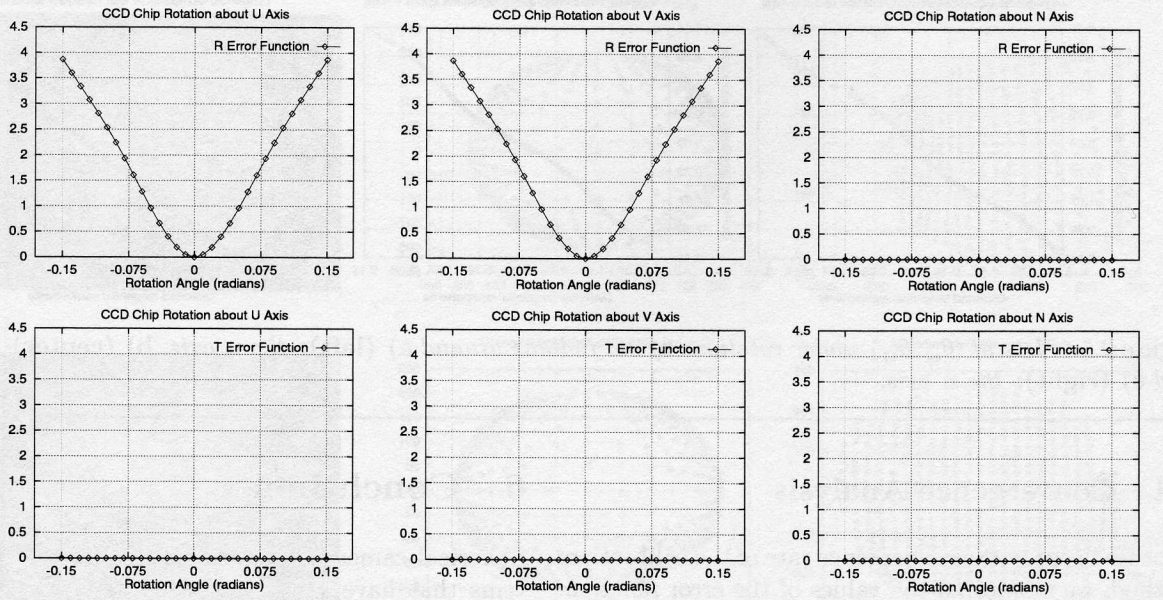

Figure 2.4: *Effect of CCD array rotation on* $\chi_r^2(\mathbf{x}_c, \mathbf{x}_p, \theta_\mathbf{u}, \theta_\mathbf{v})$ *and* $\chi_\theta^2(\mathbf{x}_c, \mathbf{x}_p)$ *functions.* **a) (top, from left to right):** *The* $\chi_r^2(\mathbf{x}_c, \mathbf{x}_p, \theta_\mathbf{u}, \theta_\mathbf{v})$ *resudual function against rotations around the* **u**, **v** *and* **n** *axes.* **b) (bottom, from left to right):** *The* $\chi_\theta^2(\mathbf{x}_c, \mathbf{x}_p)$ *residual function against rotations around the* **u**, **v** *and* **n** *axes.*

$\chi^2 = \chi_r^2(\mathbf{x}_c, \mathbf{x}_p, \theta_\mathbf{u}, \theta_\mathbf{v}) + \chi_\theta^2(\mathbf{x}_c, \mathbf{x}_p)$. In order to perform the minimization, the partial derivatives $\frac{\partial \chi^2}{\partial x_c}$, $\frac{\partial \chi^2}{\partial y_c}$, $\frac{\partial \chi^2}{\partial x_p}$, $\frac{\partial \chi^2}{\partial y_p}$, $\frac{\partial \chi^2}{\partial \theta_\mathbf{u}}$ and $\frac{\partial \chi^2}{\partial \theta_\mathbf{v}}$ need to be evaluated for various values of $(\mathbf{x}_c, \mathbf{x}_p, \theta_\mathbf{u}, \theta_\mathbf{v})$.

To evaluate the partial derivatives with respect to $\mathbf{x}_c$, we perform translations of the detected spherical calibration points $\mathbf{p}_{ij} = (r_{ij}, \theta_{ij})$ onto the image plane and perform least-squares fits to obtain the χ^2 values then used for computing 5-point central differences. Evaluation of partial derivatives with respect to CCD array angles is more involved. The first step is to reproject the pinhole calibration points $\hat{\mathbf{p}}_{ij}$ back onto the calibration plane using C^{-1}, the inverse of the pinhole camera transformation. Rotations of these reprojected points in 3D and reprojection onto the image plane of the pinhole camera provide the χ^2 values for computing 5-point central differences. The minimization is performed with the shifted and rotated calibration points and is guided by the 6D gradient vector $(\frac{\partial \chi^2}{\partial x_c}, \frac{\partial \chi^2}{\partial y_c}, \frac{\partial \chi^2}{\partial x_p}, \frac{\partial \chi^2}{\partial y_p}, \frac{\partial \chi^2}{\partial \theta_\mathbf{u}}, \frac{\partial \chi^2}{\partial \theta_\mathbf{v}})$. The output of the algorithm is the optical center $\mathbf{x}_c$, represented as the shift from the image center, the camera translation $\mathbf{x}_p$ parallel to the calibration surface with respect to the central calibration point, the CCD sensor array pitch and yaw angles $\theta_\mathbf{u}$ and $\theta_\mathbf{v}$ and the polynomials in r and θ for image transformation from spherical to pinhole. In essence, the procedure is to find the calibration parameters that best explain the detected calibration points as imaged by the spherical lens.

5 Numerical Results

We study the convergence rate of the calibration procedure and the results obtained with the calibration images of Figures 5.6a and d, corresponding to spherical cameras A and B, respectively. The calibration plane has a width and height of 8 feet and the 529 calibration dots are spaced by 4 inches both horizontally and vertically. In order to capture the calibration images, the spherical cameras are mounted on a tripod and aligned in turn with the central calibration dot.

The convergence study is performed with a simulated spherical lens. We use equation (3.8) to compute the spherical points $\mathbf{p}_{ij}$ from the synthetic pinhole calibration dots $\hat{\mathbf{p}}_{ij}$. To model CCD sensor array misalignments, we perform 3D rotations of the synthetic pinhole camera and reproject the synthetic calibration points onto the so rotated image plane prior to using (3.8). In addition, we translate the spherical calibration points $\mathbf{p}_{ij}$ to model the distance of the optical center from the center of the image and also translate the synthetic pinhole calibration points $\hat{\mathbf{p}}_{ij}$ to model the camera translation parallel to the calibration surface.

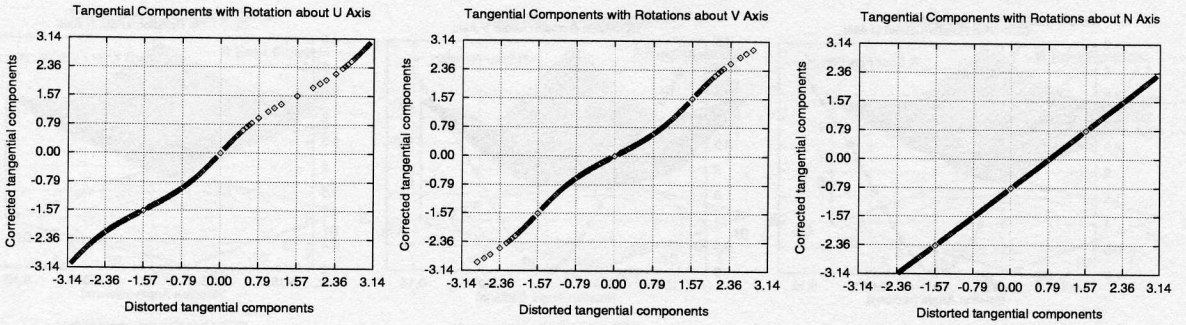

Figure 2.5: *Plots of* $(\hat{\theta}_{ij}, \theta_{ij})$ *under rotations of 0.8 radians around* **a) (left):** *the* **u** *axis,* **b) (center)** *the* **v** *axis and* **c) (right):** *the* **n** *axis.*

5.1 Convergence Analysis

In order to study the convergence rate of the calibration method, we monitored the values of the error function χ^2 with respect to the number of iterations performed in the minimization procedure using the Polak-Ribiere conjugate gradient technique. As expected, the number of required iterations to converge to the solution is proportional to the distance of the calibration parameters to the initial search values. We used a tolerance of 1×10^{-8} on convergence and we computed the various derivatives of the error function χ^2 with 5-point differences with intervals of 0.2 image units for translation and intervals of 0.0002 radians for rotations. Our experiments demonstrate that convergence rates are steep and, in general, 40 to 60 iterations are sufficient to obtain adequate calibration parameters.

5.2 Calibration of Spherical Images

We have applied our calibration procedure to both of our spherical cameras and determined their calibration parameters. Figure 5.6 shows the calibration images, the spherical points detected from them, and the polynomial reconstruction of those detected points.

As figure 5.6c demonstrates, our spherical camera A has a serious assembly misalignment. The yaw angle is in excess of 0.16 radians. However, spherical camera B does not suffer from such misalignments and Figure 5.6f shows a quasi fronto-parallel polynomial reconstruction of the detected spherical calibration points. In the case of camera A, the misalignment of the CCD array is visible by careful visual examination of the device. However, these misalignments can be easily corrected by appropriate rotations of the points to compensate for the pitch and yaw angles of the CCD sensor array.

6 Conclusion

Spherical cameras are variable-resolution imaging systems that have been recognized as promising devices for autonomous navigation purposes, mainly because of their wide viewing angle which increases the capabilities of vision-based obstacle avoidance schemes. In addition, spherical lenses resemble the primate eye in their projective models and are biologically relevant. We presented a novel method for spherical-lens camera calibration which models radial and tangential distortions of the lens and determines the optical center and the angular deviations of the CCD sensor array within a unified numerical procedure. Contrary to other methods, there is no need for special equipment such as low-power laser beams or non-standard numerical procedures for finding the optical center. Numerical experiments are presented and the results have shown adequate convergence rates. The method was successfully applied to our pair of spherical cameras and allowed us to diagnose a severe CCD array misalignment of camera A.

References

[1] R. L. Anderson, N. Alvertos, and E. L. Hall. Omnidirectional real time imaging using digital restoration. *SPIE High Speed Photograph*, 348, 1982.

[2] S. Baker and S. K. Nayar. A theory of catadioptric image formation. In *Proceedings of ICCV*, pages 35–42, Bombay, India, January 1998.

[3] A. Basu and S. Licardie. Alternative models for fish-eye lenses. *Pattern Recognition Letters*, 16(4):433–441, 1995.

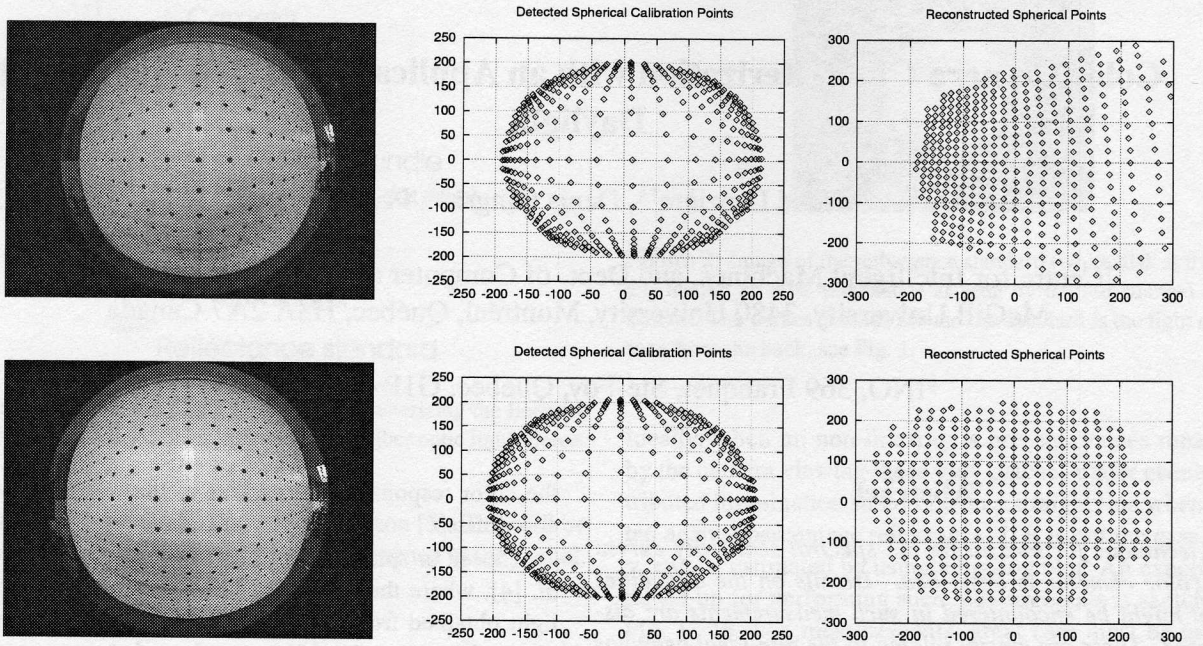

Figure 5.6: *Calibration experiment with spherical cameras A and B.* **a) (top left):** *The calibration image for camera A.* **b) (top center):** *The corresponding detected spherical points.* **c) (top right):** *The polynomial reconstruction obtained for this set of calibration points.* **d) (bottom left):** *The calibration image for camera B.* **e) (bottom center):** *The corresponding detected spherical points.* **f) (bottom right):** *The polynomial reconstruction obtained for this set of calibration points.*

[4] Y. Kuniyoshi, N. Kita, and K. Sugimoto. A foveated wide angle lens for active vision. In *IEEE Proceedings Robotics and Automation*, 1995.

[5] K. Myiamoto. Fish eye lens. *J. Lett.*, pages 1060–1061, 1964.

[6] Y. Nomura, M. Sagara, H. Naruse, and A. Ide. Simple calibration algorithm for high-distortion-lens camera. *IEEE PAMI*, 14(11):1095–1099, 1992.

[7] American Society of Photogrammetry. *Manual of Photogrammetry, 4th edition.* 1980.

[8] E. Polak. *Computational Methods in Optimization.* Academic Press, New-York, 1971.

[9] S. Shah and J. K. Aggarwal. Autonomous mobile robot navigation using fish-eye lenses. *Image Analysis Applications and Computer Graphics*, 1024:9–16, 1995.

[10] S. Shah and J. K. Aggarwal. Intrinsic parameter calibration procedure for a (high distortion) fish-eye lens camera with distortion model and accuracy estimation. *Pattern Recognition*, 29(11):1775–1778, 1996.

[11] S. Shah and J. K. Aggarwal. Mobile robot navigation and scene modeling using stereo fish-eye lens system. *Machine Vision and Applications*, 10(4):159–173, 1997.

[12] S. W. Shih, Y. P. Hung, and W. S. Lin. When should we consider lens distortion in camera calibration. *Pattern Recognition*, 28(3):447–461, 1995.

[13] R. Y. Tsai. A versatile camera calibration technique for high-accuracy 3d machine vision metrology using off-the-shelf tv cameras and lenses. *IEEE Journal of Robotics and Automation*, 3(4):323–344, 1987.

[14] J. Weng, P. Cohen, and M. Herniou. Camera calibration with distortion models and accuracy evaluation. *IEEE PAMI*, 14(10):965–980, 1992.